Verifying Methane Inventories and Trends With Atmospheric Methane Data

Authors: John R. Worden[1], Sudhanshu Pandey[1], Yuzhong Zhang[2,6], Daniel H. Cusworth[4], Zhen Qu[2], A. Anthony Bloom[1], Shuang Ma[1], Joannes D. Maasakkers[5], Brendan Byrne[1], Riley Duren[4], David Crisp[1], Deborah Gordon[7], and Daniel J. Jacob [2]

1) Jet Propulsion Laboratory / California Institute for Technology
2) Harvard University
3) California Institute for Technology
4) University of Arizona
5) SRON Netherlands Institute for Space Research
6) Key Laboratory of Coastal Environment and Resources of Zhejiang Province, School of Engineering, Westlake University, Hangzhou, China University of Edinburgh
7) Rocky Mountain Institute

Corresponding Author: john.r.worden@jpl.nasa.gov

Abstract

The 2015 Paris Climate Agreement and Global Methane Pledge formalized agreement for countries to report and reduce methane emissions to mitigate near-term climate change. Emission inventories generated through surface activity measurements are reported annually or bi-annually and evaluated periodically through a "Global Stocktake". Emissions inverted from atmospheric data support evaluation of reported inventories, but their systematic use is stifled by spatially variable biases from prior errors combined with limited sensitivity of observations to emissions (smoothing error), as-well-as poorly characterized information content. Here, we demonstrate a Bayesian, optimal estimation (OE) algorithm for evaluating a state-of-the-art inventory (EDGAR v6.0) using satellite-based emissions from 2009 to 2018. The OE algorithm quantifies the information content (uncertainty reduction, sectoral attribution, spatial resolution) of the satellite-

based emissions and disentangles the effect of smoothing error when comparing to an inventory. We find robust differences between satellite and EDGAR for total livestock, rice, and coal emissions: 14 ± 9, 12 ± 8, -11 ± 6 Tg CH_4/yr respectively. EDGAR and satellite agree that livestock emissions are increasing (0.25 to 1.3 Tg CH_4/ yr / yr), primarily in the Indo-Pakistan region, sub-tropical Africa, and the Brazilian arc of deforestation; East Asia rice emissions are also increasing, highlighting the importance of agriculture on the atmospheric methane growth rate. In contrast, low information content for the waste and fossil emission trends confounds comparison between EDGAR and satellite; increased sampling and spatial resolution of satellite observations are therefore needed to evaluate reported changes to emissions in these sectors.

Significance Statement

The Bayesian inverse estimation algorithms we describe here, developed previously to quantify atmospheric composition from observations of Earth's radiation, is applied one step further to mitigate and account for the effects of imperfect observation sensitivity when comparing emissions informed by satellite atmospheric methane data to a reported inventory. These same algorithms allow us to quantify when this comparison is informative (total uncertainty is reduced) and when it is not. Deployment of these methods will become increasingly critical to use with the ever increasing number of satellite greenhouse gas observations and their utility not just for understanding the global carbon cycle, but for informing policy about best approaches for reducing emissions to mitigate climate change.

Introduction

The Paris Agreement resulted in a framework by which countries provide an accounting of their emissions reduction goals (or Nationally Determined Contribution, NDC). To track progress in achieving NDCs, countries are required to submit transparency reports, either annually or biennially depending on Annex 1 or 2 classification, to the United Nations Framework Convention on Climate Change (UNFCC) (e.g., Vandyck *et al*. 2016; Scarpelli *et al*. 2021, 2022). These reported inventories are combined every five years for the "Global Stocktake". Reported inventories are generated from "bottom-up'' approaches that relate activity data (e.g.,

number of livestock) and emission factors to emissions. However, emissions and their uncertainties are poorly characterized in many parts of the globe where activity measurements are not rigorously made or tested across multiple sites (Janssens-Maenhout *et al*. 2019; Scarpelli *et al*. 2021) or because emission factors vary widely within a region (Masnadi et. al., 2018; Jing et al. 2020).. Even in regions with substantial reporting infrastructure, large uncertainties for emissions can exist across fossil fuel extraction areas due to a lack of information about emission rates (e.g., Alvarez *et al*. 2018) and also because transient emissions are a substantive component of overall emission rates (Cusworth *et al*. 2022). As a consequence of the importance of this issue and the need for transparency in reported emissions and their changes, the IPCC 2019 Refinement to the 2006 IPCC Guidelines for National Greenhouse Gas Inventories states that "comparison of greenhouse gas emission estimates with atmospheric measurements" is suggested to supporting verification of bottom-up inventories (IPCC 2019). In addition, the USA National Academy of Sciences recently released a study on a "*framework for evaluating emissions inventories and information, and include several case studies for how such a framework could be applied in practice to specific sector- or country-based emission inventorie*s" (National Academies 2022).

To address the USA National Academy Recommendations, we describe in this paper a Bayesian / optimal estimation (OE) framework for verifying reported methane inventories and their trends by sector (e.g. livestock, rice, coal, waste, oil, gas). As a case study we compare methane emissions and trends for 2009 to 2018 from the EDGAR v6.0 inventory (Crippa *et al*. 2022) to emissions inverted from satellite total column atmospheric concentration data observed by the JAXA Greenhouse Gas Observing Satellite, or GOSAT (Parker *et al*. 2011; Maasakers *et al*. 2019, Zhang *et al*. 2021, Cusworth *et al*. 2021). We use EDGAR because a gridded inventory is required to compare against satellite data (Methods). We note that a country's reported inventory may simply be an integrated total for each sector; however these can be subsequently projected to a grid using prior information about emission locations (e.g. Scarpelli *et al*. 2020, 2022).

A critical component needed for verifying reported inventories with atmospheric data is the characterization and mitigation of spatially varying biases resulting from errors in the prior, combined with the limited sensitivity of the atmospheric measurements to emissions, also called "smoothing error" (Rodgers 2000). Smoothing error is typically the largest of the uncertainties in

inverse problems where the role of prior assumptions is important relative to the information content of the data used for the inverse estimate (e.g. Figure 1, Rodgers 2000). However, smoothing error is computationally challenging to quantify and consequently many global inverse estimates of greenhouse gas fluxes (e.g. Yin *et al*. 2015; Liu *et al*. 2020; Balsamo *et al*. 2021; Peng *et al*. 2022) rely on using different data sets and models to empirically assess the combined role of data and model uncertainties, and smoothing error. However, without this characterization of smoothing error, it is challenging to compare bottom-up (e.g. inventory) and top-down (inverted from concentration data) estimates, or intercompare top-down estimates, because it is unclear which of the error terms is causing observed differences.

Using the OE approach we estimate emissions by sector (Methods, Cusworth *et al*. 2021) and its information content (uncertainty reduction, smoothing error, spatial-temporal resolution of the sectoral emissions attribution, uncertainty attribution) from the GOSAT data. We show that the variable bias from smoothing error is removed in comparison between EDGAR and these satellite based emissions using the results of the OE approach. This characterization of the information content, combined with the removal of smoothing error, is demonstrably a necessary step for providing confidence when testing the spatial distribution and posited trends of sectoral emissions in reported inventories with those informed from inverse estimates of atmospheric data.

We next summarize the optimal estimation framework, how to account for smoothing error between a comparison of satellite informed estimate and inventory, and characterization of the corresponding uncertainties. Details of the OE framework are described in the methods. The results section show an information content analysis of the satellite-based estimates (by sector) and its comparison to EDGAR as well as the spatial distribution of these comparisons. In particular we focus on evaluating where the satellite data has the information to robustly test the trends posited by EDGAR and its spatial distribution and where it does not. These comparisons provide new results about agricultural emissions and trends and their spatial distribution, updated interpretation to many recent results involving GOSAT data, and identifies where new observations are needed to reduce uncertainties in the global methane budget.

Summary of Optimal Estimation Framework: As described in the seminal work of Rodgers (2000), an estimate can be described as a function of the "true state" corresponding to the

estimate ($\mathbf{z}$), its prior $\mathbf{z_A}$, the effect of noise "$\mathbf{n}$" of the measurement used to quantify the estimate $\boldsymbol{\delta_n}$, and any systematic errors $\boldsymbol{\delta_m}$ such as from the data or atmospheric model used to invert concentrations to emissions:

$$\hat{\mathbf{z}} = \mathbf{z_A} + \mathbf{A}(\mathbf{z} - \mathbf{z_A}) + \boldsymbol{\delta_n} + \boldsymbol{\delta_m} \quad (1)$$

Note that we don't perfectly know the "true state", noise vector, or the systematic errors but it is useful to write the estimate in this form as it demonstrates how these terms affects the estimate, and makes the description simpler when comparing an independent measurement (or inventory) to the estimate as shown later. The $\mathbf{A}$ is the "averaging kernel" matrix, a function of the prior ($\mathbf{Z_A}$) and posterior ($\hat{\mathbf{Z}}$) error covariances and a metric for the increase in information via the reduction in uncertainty:

$$\mathbf{A} = \mathbf{I} - \hat{\mathbf{Z}}\mathbf{Z_A}^{-1} \quad (2)$$

and also describes the sensitivity of the estimate to the true state: $\mathbf{A} = \frac{\partial \hat{\mathbf{z}}}{\partial \mathbf{z}}$ (Rodgers 2000).

As the averaging kernel matrix contains the sensitivity of the estimate to all other emissions, and other terms estimated as part of the inversion, it also describes the limited sensitivity and spatial resolution of the estimate, which is why the smoothing error (the effect of the prior assumptions and limited sensitivity on the estimate), or $\mathbf{z_A} + \mathbf{A}(\mathbf{z} - \mathbf{z_A}))$ becomes smaller as the sensitivity increases as shown in Figure 1.

Comparing an Independent Inventory to Satellite Based Emissions Estimate: To account for smoothing error when comparing an inventory to the satellite estimate we first pass the inventory (denoted as $\mathbf{z_i}$ with uncertainty $\boldsymbol{\delta_i}$, and which must be on the same gridding as the prior $\mathbf{z_A}$) through the first part of equation 1:

$$\hat{\mathbf{z}}_i = \mathbf{z_A} + \mathbf{A}(\mathbf{z_i} - \mathbf{z_A}) = \mathbf{z_A} + \mathbf{A}(\mathbf{z} - \mathbf{z_A} - \boldsymbol{\delta_i}) \quad (3)$$

For future reference we describe this operation as "applying the observation operator". The approach follows that used to compare satellite based composition measurements to independent data sets such as ozone-sondes (e.g., H. Worden et al. 2007) or up-looking Fourier Transform Spectrometers (e.g. Wunch et al. 2016).

After application of equation 3 to the inventory, a comparison of the emissions modified by the observation operator with the satellite based emissions (by sector) is given by:

$$\hat{\mathbf{z}} - \hat{\mathbf{z}}_i = \mathbf{A}(\boldsymbol{\delta}_i) + \boldsymbol{\delta}_n + \boldsymbol{\delta}_m \quad (4)$$

The effect of the *a priori* assumptions from $\mathbf{z_A}$, is now removed, mitigating the effect of smoothing error (see methods for smoothing error calculation) on this comparison so that the inventory can be compared to the satellite based emissions without this large, spatially varying bias affecting the comparison. The error of the difference between satellite estimate and this adjusted inventory is then the variance of the difference:

$$E||\hat{\mathbf{z}} - \hat{\mathbf{z}}_i|| = \mathbf{A}\mathbf{S_i}\mathbf{A}^{\mathbf{T}} + \mathbf{S_n} + \mathbf{S_m} \quad (5)$$

Where $\mathbf{S_i}$, $\mathbf{S_n}$, and $\mathbf{S_m}$ are the error covariances for the inventory, observation uncertainty, and systematic errors, and can be explicitly calculated or approximated (Methods) and then used to evaluate the difference between satellite based emissions estimate and an inventory. Equation 5 shows that, while the spatially varying bias from errors in the prior $\mathbf{z_A}$ are removed with this comparison approach, the comparison still depends on the sensitivity of the estimate via the averaging kernel matrix. Smoothing error, which includes the effect of imperfect sensitivity, is therefore mitigated but not completely removed in this comparison.

Results

Use Case: As a demonstration of how this Bayesian / OE approach can be used to evaluate a reported inventory using satellite data, we compare sectoral emissions (and trends) from an OE based emissions estimate using total column methane data from the GOSAT satellite (Parker *et al*. 2011) to those from EDGAR version 6.0 (Methods). The satellite emissions are in part based

on methane fluxes derived in a previous study (Zhang *et al*. 2021) and then the fluxes are projected to emissions and trends by sector using an OE based sectoral partitioning algorithm (Methods, Cusworth *et al*. 2021). The information content of this estimate (averaging kernel, prior and posterior covariances, and estimate of observation and systematic errors) are all provided with this estimate (Methods) and used with the comparison to EDGAR.

We use EDGAR 6.0 as it is a gridded inventory that is different from the priors used in the satellite based estimate (Methods) and is therefore relatively straightforward to demonstrate how the information content of the satellite based emissions estimates can test the emissions and trends posited by EDGAR 6.0. However, the approaches described here can also be used to evaluate any inventory and its trends that might be reported and requires evaluation, e.g., as part of the Global Stocktake, and then gridded so that it can be compared to the satellite estimates (e.g. Scarpelli *et al*. 2020, 2022). We next describe comparisons between the satellite based estimates and EDGAR when integrated over the whole globe, the information content of this comparison, and then how this information is spatially distributed by sector.

Comparison of Integrated Sectoral Emissions and Trends between EDGAR and Satellite: The total global emissions from EDGAR 6.0, the effect of the observation operator (Equation 3) on EDGAR, and the sectoral emissions estimates based on GOSAT data, as well as the prior used for the GOSAT based sectoral emissions estimates are shown in Figure 2a. Trends for each sector are shown in Figure 2b. The uncertainties for each of these integrated quantities account for the cross-terms between elements of the state vector (Methods). As discussed further in Methods, the state vector includes emissions and their trends by sector, as well as wetland fluxes for each month, and the methane chemical sink (OH). After applying the gridded observation operator to EDGAR as described in Methods, the emissions and trends by sector are integrated for the whole globe and shown in Figures 2a and 2b.

The conclusions about the integrated emissions are essentially the same as those inferred from the integrated fluxes that they are based upon and described in a previous manuscript (Zhang *et al*. 2021). However, there are some differences about the trends between these previously published results and those shown in Figure 2; notably the rice, waste, and the oil and gas (O&G) trends are smaller, likely because the priors for the sectoral attribution of the emissions are different. In addition, a "relative weighting" approach is used in this previous

study to scale integrated methane fluxes in each grid to emissions, and this approach does not account for the prior distribution and posterior errors of the emissions that are used in our OE based sectoral attribution approach (Methods).

Information Content Analysis: How Applying the Observation operator to EDGAR Informs Interpretation of the Satellite / EDGAR Comparison*:* Applying the observation operator to an independent inventory accounts for the smoothing error, and when compared to the satellite-based estimate, removes the spatially variable bias due to errors in the choice of prior (Equation 4). As shown by Equation 5, the EDGAR inventory (modified with observation operator) and satellite based estimates therefore agree if the orange line overlaps (1-sigma) with the GOSAT (red) estimate. However, agreement does not necessarily mean accurate because the satellite-based estimate and modified EDGAR can agree if the sensitivity is zero such that both simply represent the choice of prior.

Smoothing error includes not just the error in the prior for the quantity of interest (e.g. livestock emissions) but also its dependency of other elements of the state vector that affect this estimate. Figure 2c shows the averaging kernel matrix for the integrated quantities shown in Figures 2a and 2b. The row of the averaging kernel matrix describes the sensitivity of the diagonal to the true distribution of the other elements of the state vector (recall that $\mathbf{A} = \frac{\partial \hat{\mathbf{z}}}{\partial \mathbf{z}}$) . The column shows how perturbing that diagonal element of the state vector affects all other state vector elements (Rodgers 2000; Bowman 2007). Figure 2c also includes the state vector elements representing wetlands and the chemical sink (WL and OH) that are jointly estimated (Zhang *et al*. 2021) with the anthropogenic emissions. For example, the total livestock emissions depend substantively on the total waste and rice emissions and the chemical sink, or as shown in Equation 1 the difference between the "true value" of these quantities and their priors (or error in the priors). While the total livestock emissions estimate also depends on the trends in livestock, waste, O&G, and fires and geological emissions (LT, WT, OGT, and FGT), in practice these cross-terms should not contribute much to the livestock emissions estimate because their values are much smaller as seen by comparing Figure 2b with 2a. Applying the observation operator to the inventory removes the effect of these cross-terms on the comparison with the satellite estimate as shown in Equation 4.

Information Content Analysis: Description of DOFS: Contained in Figure 2a and 2b is a parameter called "DOFS" or degrees of freedom for signal which describes the number of independent pieces of information for an estimate (Rodgers 2000). DOFS is calculated from the trace of the sub-matrix of the averaging kernel corresponding to each sector. A value of 0 means no sensitivity to the underlying emissions whereas increasing DOFS means increasing sensitivity. Although each sector generally has a DOFS larger than one, these DOFS are distributed over many geographical regions (see supplemental Figures). Nonetheless, this is a useful metric for assessing how much information is available for an observing system for each sector, especially if the DOFS are very small, indicating little sensitivity of the estimate to the true distribution. For example, ss discussed previously, the modified inventory and satellite-based estimate can agree if the sensitivity (i.e. DOFS) is zero such that both simply reflect the prior.

The DOFS in Figure 2a and 2b are not for the global total emissions (and trends) but instead reflects the information in their spatial distribution as it is based on the gridded averaging kernel matrix. For example, we expect the observing system described here (based on GOSAT data) to provide the most information about the spatial distribution of the livestock sector and the least for the coal sector based on the DOFS metric. For comparison, the diagonal value for the averaging kernel shown in Figure 2c is the DOFS for the integrated totals shown in Figures 2a and 2b. Comparison of the DOFS in Figure 2a with the diagonal value in Figure 2c shows how cross-correlations between elements of the state vector affect the information in the estimate. For example, once the livestock emissions for the whole globe are integrated to a single value representative of the whole globe, it actually has a lower DOFS (diagonal of averaging kernel in Figure 2c) than that for the coal or the O&G sectors because there is stronger dependency of the integrated livestock emissions estimate on other elements of the state vector. We use the DOFS metric, along with the calculated uncertainties to support interpretation of the estimates (and comparison to EDGAR) for the spatial distribution of emissions and trends in the next sections.

Livestock Emissions and Changes: As shown in Figure 2a, the largest amount of information (DOFS) from this observing system for an emissions sector, is for the spatial distribution of the livestock emissions. Based on the comparison between the modified EDGAR and satellite estimate (orange and red lines respectively), we conclude that EDGAR livestock

emissions are 15 ± 9 Tg CH_4/yr too small. Most of this discrepancy is due to underestimates of livestock emissions in East Africa and Brazil, along the arc of deforestation as shown by comparing the spatial distribution of the satellite-based estimates to EDGAR (Supplemental Figure 1).

Figure 2b shows that the trend in EDGAR 6.0 integrated livestock emissions, both before and after applying the observation operator, is consistent (within calculated uncertainties) with the satellite estimates. Figure 3 also demonstrates that the spatial distribution of this trend is broadly consistent between the EDGAR and satellite estimates, with both showing increases in emissions in Brazil, West and East sub-tropical Africa, and the Indo-Pakistan region. However, within these regions there can be substantial differences between the EDGAR and satellite-based trend estimates. Figure 3c shows one approach for using the information content from the OE based characterization for interpreting this comparison. This figure shows the ratio of the (absolute magnitude) difference from Figures 3a and 3b to the calculated uncertainty (Equation 5). Furthermore, only differences where DOFS that are larger than 0.05 (Supplemental Figure 2) are shown to ensure the corresponding observation has some sensitivity to the underlying trends (recall that $\mathbf{A} = \frac{\partial \hat{\mathbf{z}}}{\partial \mathbf{z}}$, Rodgers 2000). A value of one in Figure 2c means the difference between EDGAR and satellite is within 1-σ uncertainty.

Using this information content analysis, these comparisons provide increased confidence that observed increases in livestock emissions are larger than expected (greater than 1-σ uncertainty) along the Brazilian arc of deforestation where there is substantial conversion of forest to pasture (e.g. Morton *et al*. 2006; Xu *et al*. 2021) and subsequent use for livestock during this time period. Furthermore, we have confidence that livestock emissions are increasing in sub-tropical West and East Africa as both EDGAR and satellite agree and there is sufficient information that the agreement is not a reflection of the prior or other elements of the state vector. On the other hand, both positive and negative trends of livestock emissions are observed in the Indo-Pakistan region, which is somewhat different than EDGAR which shows only positive trends. These livestock changes, combined with slightly decreasing wetland emissions in India (Zhang *et al*. 2021), are consistent with a previous study showing nearly constant total emissions from India (Ganesan *et al*. 2017) over this same time period, although a subsequent

paper has shown decreases in emissions in this region using the same data (Wang *et al*. 2021) that is inconsistent with these results.

Because the EDGAR estimate for the livestock emission trend, after the observation operator is applied, agrees well with the satellite estimate, the original EDGAR value (~1 Tg CH_4 /yr/yr) is entirely plausible. Therefore, our final estimate for the change in livestock emissions is the low end of the satellite value to the high-end of the original EDGAR value (0.25 to 1.3 Tg CH_4/yr/yr).

Systematic errors in the data (e.g. errors related to albedo) or model (e.g. model transport and chemistry) could also potentially affect the trend in the satellite result if these vary from year to year; for example albedo can vary with different snow/surface water conditions or model transport can vary with, for example, El Nino. However, as these effects are included in the satellite and emission estimate it is more likely that these types of errors impart some year-to-year variability as opposed to longer-term temporal increases or decreases such that we do not expect these systematic errors to affect our conclusions about trends.

Oil and Gas Sector Emissions and Changes: As a contrast to the livestock sector, where there is significant information content in the comparison, we next discuss the information content of this GOSAT based observing system for evaluating the distribution of emissions and trends of the O&G sector. Note that we combine oil and gas together as they can be challenging to distinguish because of spatial overlap and frequent commonality in upstream practices (e.g. Alvarez et al, 2018, Scarpelli *et al*., 2022). Figure 2a shows the substantial role of the prior uncertainties and limited sensitivity of the satellite observations on the O&G emissions estimate. For example, the EDGAR 6.0 inventory sets total O&G emissions at around ~70 Tg CH_4/yr. After applying the observation operator to EDGAR, this value shifts downwards to ~48 Tg CH_4/yr and is consistent (within uncertainty) with the satellite observation (orange line) and its prior (black line). Because EDGAR modified by the observation operator agrees with the satellite estimate, we conclude that the satellite observations cannot falsify the higher global total posited by EDGAR (blue). On the other hand, as seen in the supplemental figures (Figures S3 and S4), this observing system can resolve total gas emissions over high emitting areas such as the Permian Basin in Texas (Zhang *et al*. 2020; Cusworth *et al*. 2021) and the Turkmenistan facilities (Varon *et al*. 2019), suggesting that most of this discrepancy is due to limited sensitivity

of the observing system in lower emitting regions that in aggregate can make up a large portion of the O&G emissions.

Figure 4 demonstrates that this observing system has less information about trends in O&G emissions. EDGAR expects large changes in these emissions across the N. Hemisphere (Figure 4a). However, these changes in EDGAR are near zero for most of the globe after applying the observation operator because the information content is small (DOFS = 2.5 for the spatial distribution for the whole globe), such that the observation operator places the EDGAR trends near the (zero) prior. As this result is consistent with the satellite data, except in regions surrounding Turkmenistan, all that can be said from this comparison is that this observation system cannot robustly verify posited trends in O&G emissions. These results demonstrate the importance of combining sensitivity analysis (e.g. DOFS) with the uncertainty calculation to determine if an atmospheric concentration informed estimate can robustly test or verify reported emissions and their trends.

Rice, Waste, and Coal Comparisons: We next summarize what we believe are the more interesting findings with respect to the comparisons between EDGAR and satellite for the rice, waste, and coal sectors, and their trends. The supplemental contains the spatial distribution (at 4x5 lon/lat gridding) for the EDGAR emissions and trends for each sector, EDGAR after the observing operator is applied, the satellite based estimate, the DOFS, and the equivalent of Figure 3c for each of the emissions and corresponding trend. We refer the reader to these Supplemental figures for the subsequent discussion.

Rice: The spatial distribution for rice emissions is consistent (within the calculated uncertainty) between satellite and EDGAR (with observation operator applied) for almost all grid cells and within 1.5 σ uncertainty (12 ± 8 Tg CH_4/yr) for the global total. The diagonal of the averaging kernel matrix (Figure 2c) indicates substantial sensitivity (~0.9 DOFS) for the integrated total emissions with only partial sensitivity to waste and livestock, confirming a robust estimate for total rice emissions. However, there are substantial differences between EDGAR and satellite for the rice trends. For example, EDGAR posits small increases in emissions from rice farming in Africa, Indonesia, India and East Asia, but a decline in South-East Asia (Supplemental Figure S6). However, after applying the observation operator to EDGAR, the small decline in rice emissions in SE Asia becomes a slight positive increase; this adjusted EDGAR is still ~2.5 smaller (relative to the uncertainty) of the satellite data, indicating that an

increase in rice emissions in this region is likely. On the other hand, while the observed emissions from rice in China are larger than EDGAR (after adjusting with the observation operator), the difference is within the uncertainty; hence we conclude that rice emissions in China are likely increasing. Combined with the results on livestock emissions, these comparisons highlight both the importance of agriculture in affecting the growth rate of atmospheric methane and also the need for accounting for smoothing error when interpreting differences between top-down and bottom-up estimates.

Coal: As with rice emissions, the spatial distribution and the integrated emissions for coal are mostly in agreement between EDGAR (with observation operator applied) and observed. Significant sensitivity to total coal emissions (Figure 2c) and minimal dependency on cross-terms in the state vector supports the robustness of this result. However, as shown in the supplemental figures (Supplemental Figure S8), a negative trend in the EDGAR N. China coal emissions is replaced with a slight positive trend once the observation operator is applied, likely because of the role of the waste trend on the trends for coal as shown by the averaging kernel matrix in Figure 2c. These large differences between the original EDGAR values and the EDGAR with observation operator, highlight how correlations in the observing system can alter the interpretation, or add additional context to a conclusion. For example, previous results also based on GOSAT data indicate a large increase in coal emissions in N. China, despite stated decreasing inventories (Miller *et al*. 2019; Sheng *et al*. 2021), consistent with the results shown here. However, the characterization provided by the optimal estimation approach suggest that at least part of this observed increase result from spatial correlations in the inversion as demonstrated by Figure 2c (Zhang *et al*. 2022). Consequently, a more robust conclusion is that the posited EDGAR decline in coal is too steep but a slight decrease in coal emissions cannot be falsified.

Waste: These comparisons also demonstrate that waste emissions and their trends (Supplemental Figures 9 and 10) are not well tested with this observing system as the information content is low (DOFS ~0.4 for total emissions as seen in Figure 2c). The row of the averaging kernel matrix also shows strong dependency of waste emissions on emissions from livestock, rice, and coal. These results indicate that the waste estimate strongly depend on the choice of prior and explains why these results, in which the prior depends on both wastewater and landfills, are different from those in Worden *et al*. (2022) where the prior only depends on

landfills; essentially the integrated estimate for waste is primarily dependent on the prior because the diagonal of the averaging kernel matrix is less than 0.5 Similarly, trends in waste emissions are not well resolved because of low information content. Higher resolution estimates are therefore needed to resolve this sector's emissions and trends from other sectors (e.g. Maasakkers *et al*. 2022).

Summary and Future Directions

The Global Methane Pledge and recent Conference of Parties stresses the increasing need for evaluating a countries reported methane emissions and changes with atmospheric observations to support methane emission reduction efforts, for the purpose of mitigating near term climate change. In turn, the recent USA National Academy report emphasizes the need for a framework and corresponding use-cases that includes atmospheric measurements for providing robust information about GHG emissions and their changes (National Academy 2022). There are also nascent efforts to develop these information systems, that are based on satellite atmospheric concentration data such, as the European Copernicus project (COCO2 2022), as well as substantive discussion on this subject across the science communities in previous and current conferences (e.g. WMO 2023) . As demonstrated by the use case in this manuscript, optimal estimation provides a framework and characterization approach for robustly comparing satellite emissions to an independent inventory. The benefits of OE include 1) evaluation of the information content of the satellite top-down estimates which in turn allows us to determine where the comparison has information and where it does not, 2) improved confidence in comparisons between the satellite and inventory emissions as one of the largest uncertainties in the comparisons, smoothing error, is accounted for in the comparison and mitigated, 3) additional context in interpreting the spatial and temporal distribution of emissions via evaluation of the averaging kernel and posterior covariances, 4) a theoretical framework for attributing different sources of uncertainty, and 5) identifying where additional measurements are needed to resolve emissions and their changes.

For our use case, we compare emissions and trends from 2009 to 2019 from an observation system based on the satellite GOSAT data, the GEOS-Chem model, and choice of constraints (Zhang *et al*. 2021), with emissions and trends from the EDGAR v6.0 methane

inventory. We find that this observing system has the most information about the spatial distribution of livestock emissions and trends such that we are confident that EDGAR livestock emissions are underestimated but that posited increases in livestock emissions by EDGAR are consistent with satellite observed increases (0.25 to 1.3 Tg CH_4/ yr / yr), primarily in the Indo-Pakistan region, Africa, as well as the Brazilian arc of deforestation where there has been substantial conversion of forest for agricultural use in the last two decades (Xu *et al*. 2021). A smaller contribution from rice emissions in China and SE Asian also likely contributes to increasing methane; combined these results highlight the importance of food production on the global methane budget (e.g. Crippa *et al*. 2021) and its growth rate.

Because we calculate the information content of these estimates we can determine where the comparisons are meaningful (total uncertainties are reduced) and where they are not. For example, large regional changes in O&G emissions posited by the EDGAR inventory cannot be tested with this satellite data set because of low information content of the observing system for this sector. An observing system will therefore need increased spatial-temporal resolution to evaluate a countries reported fossil emissions (e.g. Scarepelli *et al*. 2022) and their Nationally Determined Contribution to the UNFCCC.

The information content (sensitivity and uncertainties) and corresponding spatial-temporal resolution of an observing system is largely driven by observation density and prior error covariance. The TROPOMI satellite instrument is now providing ~100x higher observation density than the GOSAT instrument used in this work, although there are still some artifact issues affecting its use in global inversions (Qu et al., 2021; Barré et al., 2021). As these artifact issues get resolved (Lorente et al., 2021) and new instruments are launched (Jacob et al., 2022), we can expect the information content on methane fluxes from satellite observations to increase considerably. Multiple observations have found that high emitters at small scales (10s of meters) can make outsized contributions to regional (100's of km) methane fluxes (e.g. Frankenberg *et al*. 2016; Varon *et al*. 2019, 2022; Cusworth *et al*. 2022; Maasakkers *et al*. 2022). Combining observations that map methane enhancements at sub-kilometer scale (e.g. GHGSat, Carbon Mapper, Sentinel-2, EMIT) over intensely emitting facilities, with the global mapping available from other satellite instruments will therefore be critical for enabling climate action. The OE framework described here also provides the underlying theory for a greenhouse gas information

system that can integrate these data sets with their vastly different spatial scales and use them to test and update reported inventories in a fully Bayesian manner.

Methods

Background on Satellite Based Emissions by Sector: The sectoral emissions and trends inverted from the satellite data are derived in a two step process. The first step is described in previously published results and comprises a global inversion using total atmospheric column methane data from the Japanese GOSAT (Greenhouse gases Observing SATellite) instrument (Parker *et al*. 2011) and the GEOS-Chem model (Zhang *et al*. 2021). The state vector for this inversion include 1) integrated anthropogenic methane fluxes between 2010 and 2018 at a gridding of 4x5degrees (latitude/longitude), 2) the corresponding linear trend for these years, 3) wetland methane emissions for specified regions for each month between 2010 and 2018), and 4) the yearly methane sink. We refer the reader to the paper by Zhang *et al*. (2021) for a full description and evaluation of this inversion. The second step is a linear estimate of emissions by sector (and their trends) based on an optimal estimation sectoral emissions attribution approach (Methods, Cusworth *et al*. 2021; Worden *et al*. 2022) that projects the integrated anthropogenic fluxes and trends to emissions by sector and trends at the same 4x5 gridding. The emissions state vector includes livestock, waste (landfills and wastewater), rice, coal, O&G, and fires and geological. The state vector also includes the trends for these emissions as well as the wetlands and OH state vector from the flux inversion in the first step. This OE based projection from integrated anthropogenic fluxes to emissions by sector accounts for the prior distribution and uncertainties in the emissions, and includes the effects of the jointly estimated wetland fluxes and methane sink. Furthermore, because the posterior covariance is generated from this step (Methods, subsequent section), we can calculate an averaging kernel matrix which is then used to create the "observation operator" for the emissions and trends by sector as shown by Equation 2 in the main text.

EDGAR Inventory and Uncertainties: We use the v6.0 EDGAR inventory (Crippa *et al*. 2020). The inventory is first projected to the 4x5 degrees (lat/lon) gridding used with the satellite based emissions estimates. Critical towards comparing a gridded inventory with inversely estimated

emissions is a realistic *a priori* error covariance that describes their uncertainties and any correlations between adjacent emissions. Because EDGAR does not provide an error covariance for its emissions, we use the prior covariances that were previously generated for use by the satellite based emissions estimate by sector (Worden *et al*. 2022, Methods) as a convenience to simplify the demonstration of the information content calculations.

***Optimal Estimation Description*:** The OE framework, used for comparing the satellite based sectoral emissions and trend to an independent methane inventory, follows the approach in Rodgers seminal work "Inverse methods **for atmospheric sounding: theory and practice**" (Rodgers 2000), and used extensively in remote sensing of methane and other atmospheric trace gases (e.g. Worden *et al*. 2004; B*et al*.*et al*. 2*et al*.arker *et al*. 2011). Here we provide a more in-depth derivation of the basic OE equations than discussed previously in the main text summary.

The estimate for each Imission type and its trends can be written as a function of the true state for these parameters ($\mathbf{z}$), its prior $\mathbf{z_A}$, the noise "$\mathbf{n}$" of the measurement used to quantify the fluxes, and any systematic errors $\boldsymbol{\delta_m}$:

$$\hat{\mathbf{z}} = \mathbf{z_A} + \mathbf{A}(\mathbf{z} - \mathbf{z_A}) + \mathbf{Gn} + \boldsymbol{\delta_m} \quad (1)$$

Note that this is the same as Equation 1 in the main text except that we replace $\boldsymbol{\delta_N}$ with $\mathbf{Gn}$. The posterior error covariance for this estimate, or Hessian, $\hat{\mathbf{Z}}$ is the weighted sum of the prior uncertainties or covariance $\mathbf{Z_A}$, and the information from the observations ($\mathbf{K}^T\mathbf{S_n}^{-1}\mathbf{K}$):

$$\hat{\mathbf{Z}} = \left(\mathbf{M}^T(\mathbf{K}^T\mathbf{S_n}^{-1}\mathbf{K})\mathbf{M} + \mathbf{Z_A}^{-1}\right)^{-1} \quad (2)$$

The "Jacobian" $\mathbf{K}$ in Equation 2 describes the sensitivity of the integrated methane flux (or trend) to the observed methane concentrations in each state vector element (e.g. the state vector denoted in Figure 2c but on the spatio-temporal grid described in the main text). The gain matrix $\mathbf{G}$ is a matrix containing partial derivatives that relate parameters in the observation state vector (or "$\mathbf{n}$" using the nomenclature in Equation 2) to parameters in the estimate state vector (or "$\mathbf{z}$" using the nomenclature in Equation 2) and is defined for this problem as $\mathbf{G} = \hat{\mathbf{Z}}(\mathbf{MK})^T\mathbf{S_n}^{-1}$

(Bowman *et al*. 2007). The mapping matrix **M** describes the mapping relationship between the integrated flux (**x)** at each grid cell to the sectoral emissions that make up the flux in that grid (**x = Mz,** see subsequent Methods section on sectoral attribution**)**. The information about the fluxes from the observations described by the Jacobians **K** in Equation 2 is mapped to each sector (e.g. coal, waste, gas via the mapping matrix, and then weighted further by the prior error covariance of that sector ($\mathbf{Z_A}$) as discussed in the next section. We note that the Jacobians in Equation 2 can be further mapped to the Jacobians in the optimal estimate step used to relate observed satellite spectral radiances to methane concentrations (Parker *et al*. 2011), so that the Hessian matrix shown in Equation 2 preserves the information from the original satellite observations.

Quantifying Uncertainties: The Hessian matrix, or posterior error covariance in Equation 2, can also be written as the sum of the smoothing and observation error (Rodgers 2000, Worden *et al*. 2004; Bowman *et al*. 2007):

$$\hat{\mathbf{Z}} = (\mathbf{I} - \mathbf{A})\mathbf{Z_A}(\mathbf{I} - \mathbf{A})^{\mathbf{T}} + \mathbf{G}\mathbf{S_n}\mathbf{G}^{\mathbf{T}} \quad (3)$$

$\mathbf{Z_A}$ describes the prior error covariance for the elements in the state vector (see subsequent methods section). The first term on the right is the characterization of the smoothing error and the second term is the measurement error, or the effect of observation noise on the estimate.

The uncertainties we report for an estimate are derived from the posterior covariances. For example, if we report an individual element of the covariance (e.g. total error for a sectoral emission for a certain grid point as shown in the supplemental), then the uncertainty is simply the corresponding square root of the diagonal from the covariance. If on the other hand we report an integrated quantity (e.g. sum of all livestock emissions), then the corresponding uncertainty must be projected from the total error covariance (Worden *et al*. 2022) on the 4x5 grid to the integrated quantity. For example, the total uncertainties for the satellite based uncertainties shown in Figures 2a and 2b are derived by first quantifying the posterior error covariance for the integrated quantities of the state vector described by the row in Figure 2c:

$$\hat{\mathbf{Z}}_{\boldsymbol{i}} = \begin{bmatrix} \mathbf{h_L} \\ \dots \\ \mathbf{h_{OH}} \end{bmatrix} \hat{\mathbf{Z}}_{\boldsymbol{tot}} \begin{bmatrix} \mathbf{h_L} \\ \dots \\ \mathbf{h_{OH}} \end{bmatrix}^{\mathbf{T}} \quad (4)$$

Where the rows of the matrix $\begin{bmatrix} \mathbf{h_L} \\ \dots \\ \mathbf{h_{OH}} \end{bmatrix}$ is composed of vectors the size of the row of $\hat{\mathbf{Z}}_{\boldsymbol{tot}}$ and that have a value of 1 corresponding to the indices of the sector and 0 elsewhere. The error covariance $\hat{\mathbf{Z}}_{\boldsymbol{tot}}$is the sum of the Hessian plus our estimate of the model error covariance. The indices for **h** are the same indices shown in Figure 2c that correspond to each (integrated) elements of the state vector: L, W, R, …, WL, OH. The uncertainty for each integrated sector "***i***" is then the square root of the diagonal value of the covariance $\hat{\mathbf{Z}}_{\boldsymbol{i}}$ corresponding to the sector. To calculate the averaging kernel matrix shown in Figure 2c, we apply the same operation to the Hessian $\hat{\mathbf{Z}}$ and to $\mathbf{Z}_{\mathrm{A}}$ and then recalculated the averaging kernel matrix using Equation 2 from the main text.

Sectoral attribution: The derivation for how emissions by sector are quantified from an integrated flux is described in Cusworth *et al*. (2021). The basic equations describe a linear mapping relationship between integrated anthropogenic emissions "**x**" and the emissions by sector **"z"** within a grid that compose this flux. The linear mapping we use is a simple summation of emissions within each grid:

$$\mathbf{x} = \mathbf{M}\mathbf{z}. \quad (5)$$

The solution for projecting fluxes back to emissions takes the form:

$$\hat{\mathbf{z}} = \mathbf{z}_{\mathrm{A}} + \hat{\mathbf{Z}}\mathbf{M}^{T}\hat{\mathbf{S}}^{-1}\left[\left(\mathbf{I} - \hat{\mathbf{S}}\mathbf{S}_{\mathrm{A}}^{-1}\right)(\mathbf{x}_{\mathrm{A}} - \mathbf{M}\mathbf{z}_{\mathrm{A}}) + (\hat{\mathbf{x}} - \mathbf{x}_{\mathrm{A}})\right] \quad (6)$$

where the ($\hat{\mathbf{z}}$) is the posterior emissions vector with error covariance ($\hat{\mathbf{Z}}$) and **I** is the identity matrix. Here $\mathbf{S}_{\mathrm{A}}$ and $\hat{\mathbf{S}}$ are the prior and posterior error covariances covariance for the fluxes corresponding to the state vector **x** as described in Zhang *et al*. (2021).

Equation 6 is similar to the "prior" swapping approach used extensively for remote sensing (e.g. Rodgers and Connor 2003) in which one (e.g. $\mathbf{x_A}$) prior can be swapped with another (e.g. $\mathbf{Mz_A}$) if the Averaging kernel matrix is provided ($\left(\mathbf{I} - \hat{\mathbf{S}}\mathbf{S}_\mathrm{A}^{-1}\right)$ except that after the priors are swapped (the effect of the brackets in the above equation) it is then projected from "flux space" to "emissions space" (the effect of $\hat{\mathbf{Z}}\mathbf{M}^T\hat{\mathbf{S}}^{-1}$).

As shown previously, the posterior error covariance matrix $\hat{\mathbf{Z}}$ is calculated explicitly given $\mathbf{M}$, $\mathbf{S}_\mathrm{A}$, $\hat{\mathbf{S}}$, and prior emissions error covariance matrix $\mathbf{Z}_\mathrm{A}$:

$$\hat{\mathbf{Z}} = \left(\mathbf{M}^T\left(\hat{\mathbf{S}}^{-1} - \mathbf{S}_\mathrm{A}^{-1}\right)\mathbf{M} + \mathbf{Z}_\mathrm{A}^{-1}\right)^{-1} = \left(\mathbf{M}^T(\mathbf{K}^T{\mathbf{S}_\mathbf{n}}^{-1}\mathbf{K})\mathbf{M} + \mathbf{Z}_\mathrm{A}^{-1}\right)^{-1} \quad (7)$$

Note that in our previous work (Worden *et al*. 2022), the covariances had to be split into regions because the size of the state vector resulted in a matrix (Equation 7) that was too large to invert. We found, using simulations with smaller matrices, that this approach results in emissions estimates that are within uncertainty using the more accurate but much larger Hessian matrix, but changed the structure of the averaging kernel matrix, reducing the robustness of the comparison between the inventory and satellite based emissions suspect. For this reason, we now perform the matrix inversion using a state vector representative of the whole globe and not sub-regions.

***Sources of Uncertainty When Comparing Satellite Based Emissions Estimate and Trend to Inventory*:** As discussed in the main text, the different sources of error when comparing the satellite based emissions to an independent inventory are described by the variance of the difference between the satellite estimate and inventory modified by the observation operator:

$$E||\hat{\mathbf{z}} - \hat{\mathbf{z}}_i|| = \mathbf{A}\mathbf{S_i}\mathbf{A}^\mathbf{T} + \mathbf{S_n} + \mathbf{S_m} \quad (8)$$

Where $\mathbf{S_i}$ is the covariance for the inventory uncertainties $\boldsymbol{\delta_i}$, $\mathbf{S_n}$ is the observation error projected to emissions, and $\mathbf{S_m}$ is the model error. Note that the observation error, $\mathbf{S_n}$, either is directly calculated using a chain of partial derivatives that relates noise to concentration data to fluxes to

emissions, or it can be calculated by subtracting the "smoothing" or resolution error from the Hessian **Z** (Rodgers 2000)**:**

$$\mathbf{S_n} = \hat{\mathbf{Z}} - (\mathbf{I} - \mathbf{A})\mathbf{Z_A}(\mathbf{I} - \mathbf{A})^{\mathbf{T}} \quad (9)$$

We quantify the final term in Equation 8 (model error) using the "residual error" approach discussed in Zhang et al. (2021) which compares the difference of single observations and model values relative to yearly means of the observations minus the model. This yields a total observational error variance from which the contribution from the observing instrument can be subtracted to yield the model transport error variance. Application to satellite methane column observations indicates model transport error standard deviations of typically 5-10 ppb (Lu et al., 2021). However, for the purpose of this study we conservatively assume the model error is the same as the observation error $\mathbf{S_n}$, which is based on concentration errors that are ~14 ppb.

If only a partial inventory is provided, such as a countries reported emission inventory, then the errors still need to account for the spatially varying sensitivity of the estimate as described by the averaging kernel. In this case there is a "cross-state" term (Worden et al. 2004; H. Worden et al. 2007), in which the emissions and its prior uncertainties in one region affect the estimated emissions in another. Equation 5 then becomes:

$$E||\hat{\mathbf{z}} - \hat{\mathbf{z}}_i|| = \mathbf{A_i}\mathbf{S_i}\mathbf{A_i^T} + \mathbf{A_{ij}}\mathbf{S_{jj}}\mathbf{A_{ij}^T} \quad + \mathbf{S_n^{ii}} + \mathbf{S_m^{ii}} \quad (10)$$

Here the indices "ii" represents the submatrix of **A** and the covariances S corresponding to the reported countries emissions (for example), and the index "j" represents the emissions for all other parts of the inventory.

Description of Priors and Prior Covariances: Sectoral attribution for emissions based on atmospheric concentration data requires use of *a priori* emissions and prior covariances. For the optimal estimation approach described here, this means a realistic representation of $\mathbf{z_A}$ (priors) and $\mathbf{Z_A}$ (prior covariances). The priors and prior covariances and how they are used for the sectoral emissions are described in Worden *et al*. (2022) and the reader is directed to this paper

(Section 2.3 Generation of Prior Emissions, Covariances, and Uncertainties) for details. In summary, the *a priori* emissions are based on a combination of emissions inventories. Livestock emissions are based on the results of a 2013 NASA Carbon Monitoring System study (Wolf *et al*. 2017). Rice, landfill, solid waste, and waste water emissions are based on EDGAR 5.0 (Janssens-Maenhout *et al*. 2019) although the landfill and waste water emissions are combined as they are spatially correlated. Fossil emissions are based on reported emissions to the UNFCCC as part of the global stock-take (Scarpelli *et al*. 2020, 2022). Wetland emissions are based on an ensemble of wetland, semi-empirical process models (Bloom *et al*. 2017). Fires are based on emissions from the Global Fire Emissions Database version 4 (Giglio *et al*. 2014) and combined with natural seeps that are based on a 2019 inventory (Etiope *et al*. 2019). The covariances for OH are taken from Zhang *et al*. (2021).

Constructing a realistic *a priori* covariance is challenging as the matrix must be invertible (Equation 3) while realistically describing the prior uncertainties and their correlations. This challenge is amplified because the uncertainties and how they might be correlated are generally not well known (Janssens Maenhout *et al*. 2019). Our approach for constructing these covariances is described in our previous work (Worden *et al*. 2022) and is to first sub-divide the globe into eight regions which are primarily associated as an "Annex 1" or "Annex 2". Our primary constraint in calculating a prior covariance is that projecting it from its original gridding (in this previous work it is at 1x1 degree) down to a single value representative of the region, the total uncertainty should be 15% for a region primarily composed of Annex 1 countries while the value is 30% for regionsl primarily associated as "Annex 2" (Janssens Maenhout *et al*. 2019). Mechanistically this means that if we project, for example, the covariance for coal emissions for an Annex 1 region down to a single number than it will have an uncertainty very close to 15%. To achieve these result, the uncertainty at any grid cell must be quite large (~80% at 1 degree resolution) with substantial correlation with nearby emissions (~0.8 correlation with emissions within 400 km). These numbers are not unrealistic based on regional studies of uncertainties in California and Texas (Maasakkers *et al*. 2016) such that we adopt this general approach throughout the globe. Note that it is straightforward to use alternative priors and prior covariances if a researcher can provide them and has good rationale for their internal covariance structure.

The priors and prior covariances are initially calculated on a 1x1 degree grid box. For the study in this manuscript the gridding is 4x5 degrees (latitude/longitude). Consequently, we project the covariances at 1x1 to 4x5 (lat/lon) through simple interpolation. Our approach for quantifying the prior and covariance for the trends is to 1) set the prior for the trend to be zero at every grid box and 2) to set the covariance for the trend equal to 5% of the corresponding variance for the emissions at every grid, i.e., the covariance for the trend is simply the covariance for the emissions multiplied by 0.05^2. The prior covariances for each region are then mapped to the whole globe at 4x5 degrees. However, only elements of the globe that have non-zero emissions are used to keep the state vector small such that the matrix described by Equation 3 is robustly invertible (i.e. $\hat{\mathbf{Z}}\hat{\mathbf{Z}}^{-1} = \mathbf{I}$). Mechanistically, this means using only those emissions that are larger than 1% of the largest emission value on the globe. With this threshold we reduce the size of the emissions part of the state vector by ~50% but retain ~98% of the total emissions such that the revised total is within 8 Tg CH_4/yr of the ~350 Tg CH_4/yr total. We then redistribute this small remaining residual to the retained grid boxes so that the total emissions on this smaller subset is the same as the original.

Acknowledgements

Y. Zhang is funded by NSFC (42007198) and Westlake University. Part of this research was carried out at the Jet Propulsion Laboratory, California Institute of Technology, under a contract with the National Aeronautics and Space Administration.

Data Availability and Sharing

The sectoral attribution of emissions from fluxes depends on fluxes at the following data repository: https://zenodo.org/record/4052518#.Y6Oe0uzMKbg.

The priors and *a priori* covariances used to project fluxes to emissions by sector are stored here: https://cmsflux.jpl.nasa.gov/get-data/publication-data-sets/ (see paper by Worden, Cusworth, Qu *et al*. 2021 that is stored on this website.

References

R. A. Alvarez, *et al.*, Assessment of methane emissions from the U.S. oil and gas supply chain. *Science* **361**, eaar7204 (2018).

G. Balsamo, *et al.*, The CO2 Human Emissions (CHE) Project: First Steps Towards a European Operational Capacity to Monitor Anthropogenic CO2 Emissions. *Frontiers Remote Sens* **2**, 707247 (2021).

A. A. Bloom, *et al.*, A global wetland methane emissions and uncertainty dataset for. *Geosci Model Dev* **10**, 1 16 (2017).

K. W. Bowman, *et al.*, Tropospheric Emission Spectrometer: Retrieval Method and Error Analysis. *Ieee T Geosci Remote* **44**, 1297–1307 (2006).

M. Crippa, *et al.*, Food systems are responsible for a third of global anthropogenic GHG emissions. *Nat Food* **2**, 198–209 (2021).

M. Crippa, *et al.*, High resolution temporal profiles in the Emissions Database for Global Atmospheric Research. *Sci Data* **7**, 121 (2020).

COCO2 2022: (https://coco2-project.eu/data-portal)

D. H. Cusworth, *et al.*, Potential of next-generation imaging spectrometers to detect and quantify methane point sources from space. *Atmos Meas Tech* **12**, 5655–5668 (2019).

D. H. Cusworth, *et al.*, Strong methane point sources contribute a disproportionate fraction of total emissions across multiple basins in the United States. *Proc National Acad Sci* **119**, e2202338119 (2022).

D. H. Cusworth, *et al.*, Using remote sensing to detect, validate, and quantify methane emissions from California solid waste operations. *Environ Res Lett* **15**, 054012 (2020).

G. Etiope, G. Ciotoli, S. Schwietzke, M. Schoell, Gridded maps of geological methane emissions and their isotopic signature. *Earth Syst Sci Data* **11**, 1–22 (2018).

C. Frankenberg, *et al.*, Airborne methane remote measurements reveal heavy-tail flux distribution in Four Corners region. *Proc National Acad Sci* **113**, 9734–9739 (2016).

C. Frankenberg, J. Meirink, M. V. Weele, U. Platt, T. Wagner, Assessing methane emissions from global space-borne observations. *Science* **308**, 1010 1014 (2005).

A. L. Ganesan, *et al.*, Atmospheric observations show accurate reporting and little growth in Indiaâ€™s methane emissions. *Nat Commun* **8**, 1 7 (2017).

L. Giglio, J. T. Randerson, G. R. Werf, Analysis of daily, monthly, and annual burned area using the fourth-generation global fire emissions database (GFED4). *J Geophys Res Biogeosciences* **118**, 317–328 (2013).

M. Herrero, *et al.*, Greenhouse gas mitigation potentials in the livestock sector. *Nat Clim Change* **6**, 452–461 (2016).

IPCC 2019 https://www.ipcc-nggip.iges.or.jp/public/2019rf/pdf/1_Volume1/19R_V1_Ch06_QA_QC.pdf)

D. J. Jacob, *et al.*, Quantifying methane emissions from the global scale down to point sources using satellite observations of atmospheric methane. *Atmos Chem Phys* **22**, 9617–9646 (2022).

G. Janssens-Maenhout, *et al.*, EDGAR v4.3.2 Global Atlas of the three major greenhouse gas emissions for the period 1970–2012. *Earth Syst Sci Data* **11**, 959–1002 (2019).

Z. Jiang, *et al.*, Impact of model errors in convective transport on CO source estimates inferred from MOPITT CO retrievals. *J Geophys Res Atmospheres* **118**, 2073 2083 (2013).

T. Lauvaux, *et al.*, Global assessment of oil and gas methane ultra-emitters. *Science* **375**, 557–561 (2022).

J. Liu, *et al.*, Carbon Monitoring System Flux Net Biosphere Exchange 2020 (CMS-Flux NBE 2020). *Earth Syst Sci Data* **13**, 299–330 (2020).

X. Lu, *et al.*, Methane emissions in the United States, Canada, and Mexico: evaluation of national methane emission inventories and 2010–2017 sectoral trends by inverse analysis of in situ (GLOBALVIEWplus CH4 ObsPack) and satellite (GOSAT) atmospheric observations. *Atmos Chem Phys* **22**, 395–418 (2022).

S. Ma, *et al.*, Satellite Constraints on the Latitudinal Distribution and Temperature Sensitivity of Wetland Methane Emissions. *Agu Adv* **2** (2021).

J. D. Maasakkers, *et al.*, 2010–2015 North American methane emissions, sectoral contributions, and trends: a high-resolution inversion of GOSAT observations of atmospheric methane. *Atmos Chem Phys* **21**, 4339–4356 (2021).

J. D. Maasakkers, *et al.*, Global distribution of methane emissions, emission trends, and OH concentrations and trends inferred from an inversion of GOSAT satellite data for 2010–2015. *Atmos Chem Phys* **19**, 7859–7881 (2019).

J. Maasakkers, *et al.*, Using satellites to uncover large methane emissions from landfills. *Science Advances* (2022) https:/doi.org/10.31223/x5n33g.

M. S. Masnadi, *et al.*, Global carbon intensity of crude oil production. *Science* **361**, 851–853 (2018).

J. R. McNorton, *et al.*, Representing model uncertainty for global atmospheric CO2 flux inversions using ECMWF-IFS-46R1. *Geosci Model Dev* **13**, 2297–2313 (2020).

S. M. Miller, *et al.*, China's coal mine methane regulations have not curbed growing emissions. *Nat Commun* **10**, 303 (2019).

D. C. Morton, *et al.*, Cropland expansion changes deforestation dynamics in the southern Brazilian Amazon. *Proc National Acad Sci* **103**, 14637–14641 (2006).

National Academies of Sciences, Engineering, and Medicine 2022. Greenhouse Gas Emissions Information for Decision Making: A Framework Going Forward. Washington, DC: The National Academies Press. https://doi.org/10.17226/26641.

R. Parker, *et al.*, Methane observations from the Greenhouse Gases Observing SATellite: Comparison to ground-based TCCON data and model calculations. *Geophys Res Lett* **38**, L15807 (2011).

S. Peng, *et al.*, Wetland emission and atmospheric sink changes explain methane growth in 2020. *Nature* **612**, 477–482 (2022).

Z. Qu, *et al.*, Global distribution of methane emissions: a comparative inverse analysis of observations from the TROPOMI and GOSAT satellite instruments. *Atmos Chem Phys* **21**, 14159–14175 (2021).

Rodgers, Clive D. Inverse methods for atmospheric sounding: theory and practice. Vol. 2. World scientific, 2000.

C. D. Rodgers, B. J. Connor, Intercomparison of remote sounding instruments . *J Geophys Res Atmospheres 1984 2012* **108**, 4116 (2003).

J. A. Rosentreter, *et al.*, Half of global methane emissions come from highly variable aquatic ecosystem sources. *Nat Geosci* **14**, 225–230 (2021).

T. R. Scarpelli, *et al.*, A global gridded (0.1∘×0.1∘) inventory of methane emissions from oil, gas, and coal exploitation based on national reports to the United Nations Framework Convention on Climate Change. *Earth Syst Sci Data* **12**, 563–575 (2020).

. R. Scarpelli, *et al.*, Updated Global Fuel Exploitation Inventory (GFEI) for methane emissions from the oil, gas, and coal sectors: evaluation with inversions of atmospheric methane observations. *Atmospheric Chem Phys* **22**, 3235–3249 (2022).

J. Sheng, *et al.*, Sustained methane emissions from China after 2012 despite declining coal production and rice-cultivated area. *Environ Res Lett* **16**, 104018 (2021).

T. Vandyck, K. Keramidas, B. Saveyn, A. Kitous, Z. Vrontisi, A global stocktake of the Paris pledges: Implications for energy systems and economy. *Global Environ Change* **41**, 46–63 (2016).

D. J. Varon, *et al.*, Satellite Discovery of Anomalously Large Methane Point Sources From Oil/Gas Production. *Geophys Res Lett* **46**, 13507–13516 (2019).
K. J. Wecht, D. J. Jacob, C. Frankenberg, Z. Jiang, D. R. Blake, Mapping of North American methane emissions with high spatial resolution by inversion of SCIAMACHY satellite data. *J Geophys Res Atmospheres* **119**, 7741–7756 (2014).

J. Wolf, G. R. Asrar, T. O. West, Revised methane emissions factors and spatially distributed annual carbon fluxes for global livestock. *Carbon Balance Management* **12**, 16 (2017).

WMO 2023: https://community.wmo.int/meetings/wmo-international-greenhouse-gas-monitoring-symposium

H. M. Worden, *et al.*, Comparisons of Tropospheric Emission Spectrometer (TES) ozone profiles to ozonesondes: Methods and initial results. *J Geophys Res Atmospheres 1984 2012* **112** (2007).

J. Worden, *et al.*, Predicted errors of tropospheric emission spectrometer nadir retrievals from spectral window selection. *J Geophys Res Atmospheres 1984 2012* **109**, D09308 (2004).

J. R. Worden, *et al.*, The 2019 methane budget and uncertainties at 1∘ resolution and each country through Bayesian integration Of GOSAT total column methane data and a priori inventory estimates. *Atmos Chem Phys* **22**, 6811–6841 (2022).

J. Worden, *et al.*, Tropospheric Emission Spectrometer observations of the tropospheric HDO/H 2O ratio: Estimation approach and characterization. *J Geophys Res Atmospheres 1984 2012* **111** (2006).

D. Wunch, *et al.*, Comparisons of the Orbiting Carbon Observatory-2 (OCO-2) XCO2 measurements with TCCON . *Atmospheric Measurement Techniques Discussions*, 1 45 (2016).

L. Xu, *et al.*, Changes in global terrestrial live biomass over the 21st century. *Sci Adv* **7**, eabe9829 (2021).

Y. Yin, *et al.*, Decadal trends in global CO emissions as seen by MOPITT. *Atmos Chem Phys* **15**, 13433 13451 (2015).

Y. Zhang, *et al.*, Quantifying methane emissions from the largest oil-producing basin in the United States from space. *Sci Adv* **6**, eaaz5120 (2020).

Y. Zhang, *et al.*, Attribution of the accelerating increase in atmospheric methane during 2010–2018 by inverse analysis of GOSAT observations. *Atmos Chem Phys* **21**, 3643–3666 (2021).

Y. Zhang, *et al.*, Observed changes in China's methane emissions linked to policy drivers. *Proc National Acad Sci* **119**, e2202742119 (2022).

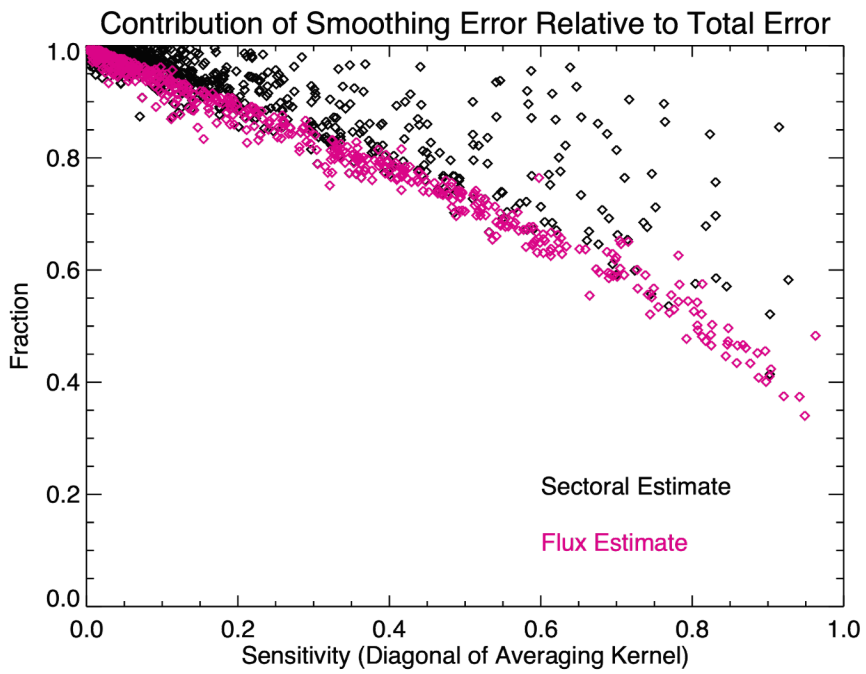

Figure 1: Smoothing error is typically the largest component of the error budget for emissions inverted from satellite data where the uncertainties in the prior are important relative to the information content of the data. Black symbols show the fraction of smoothing error relative to the total error for methane emissions (by sector) based on nine years of JAXA data on a 4x5 (lon/lat) grid. Red symbols show the fraction of smoothing error when the sectoral based emissions are integrated to a single number on each grid. As the sensitivity increases, the smoothing error becomes smaller. The total error budget includes smoothing error, error due to noise, and estimate of systematic errors (Methods).

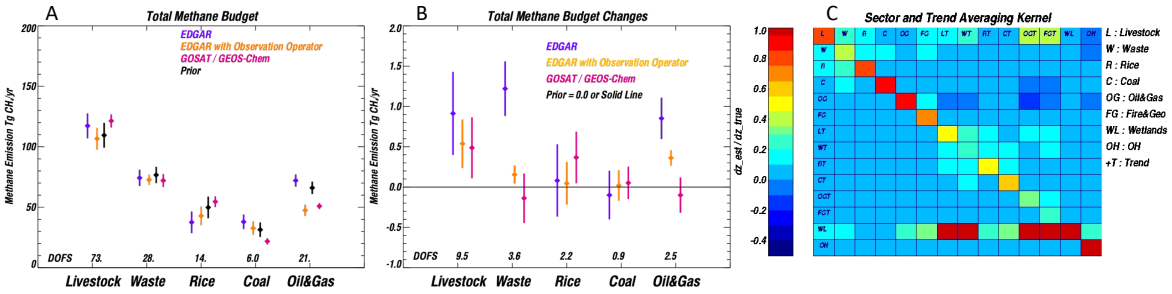

Fig. 2: (**A** / **Left**) EDGAR emissions after modification by observation operator are consistent with satellite for the Waste and Oil&Gas sectors, and inconsistent for all other sectors. (**B** / **Middle**) EDGAR inventories and satellite data agree that Livestock emissions are increasing but this observing system cannot falsify posited changes in other emissions. The DOFS (trace of Averaging Kernel Matrix) is a metric of sensitivity for the observing system and describes the number of independent pieces of information that can spatially be estimated for each sector. (**C** / **Right**). The row of this averaging kernel matrix for these integrated quantities describes the sensitivity of the estimate to the true distribution.

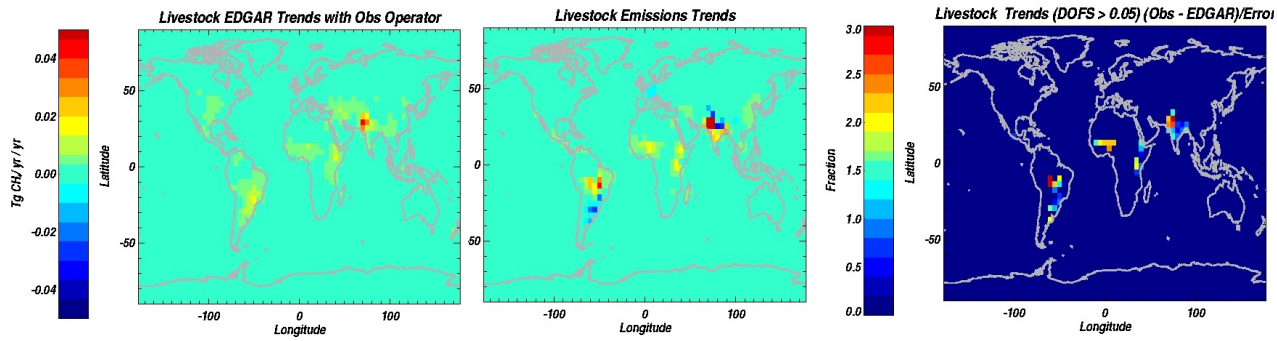

Fig. 3: (Left) The 2009-2018 trend in Livestock emissions from EDGAR, after projection through the observation operator. (Middle) Estimated change in Livestock emissions based on GOSAT satellite data. The prior for the satellite based emissions estimate is set to zero. (Right) The (absolute magnitude) difference between the satellite estimate (middle) minus the Livestock estimate (left), normalized by the error for grids where DOFS are larger than 0.05. These comparisons demonstrate that livestock emissions are likely increasing in sub-tropical Africa, Brazil along the arc-of-deforestation, and the Indo-Pakistan region.

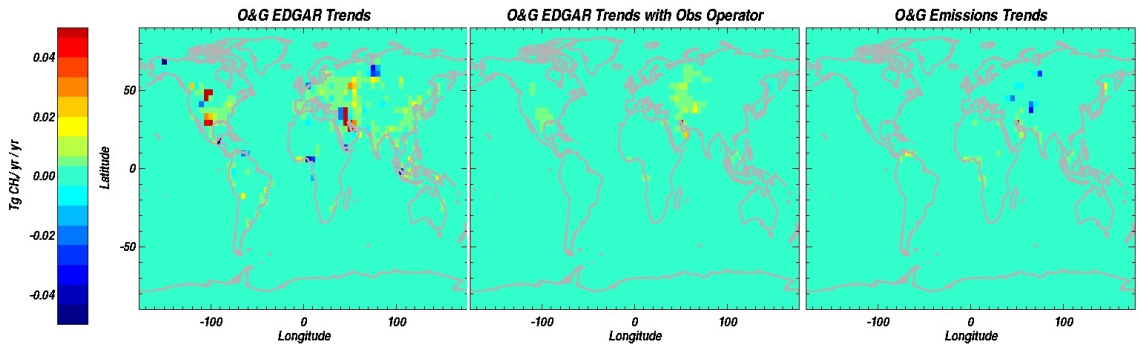

Fig. 4: (**Left**) Large trends across the globe are posited for 2009 to 2018 by EDGAR. (**Right**) The satellite observations suggest little changes in oil and gas except a possible decrease in Russia and Turkmenistan emissions in sharp contrast to EDGAR. (**Middle**) Observed lack of trends could simply be due to lack of sensitivity as projecting EDGAR through the observation operator removes most of the posited changes.